ACSNANO

www.acsnano.org

ARTICLE

Multimaterial Self-Aligned Nanopatterning by Simultaneous Adjacent Thin Film Deposition and Etching

Seung Keun Song, Jung-Sik Kim, Hannah R. M. Margavio, and Gregory N. Parsons*

Cite This: *ACS Nano* 2021, 15, 12276–12285

Read Online

ACCESS | Metrics & More | Article Recommendations | Supporting Information

ABSTRACT: Printed component sizes in electronic circuits are approaching 10 nm, but inherent variability in feature alignment during photolithography poses a fundamental barrier for continued device scaling. Deposition-based self-aligned patterning is being introduced, but nuclei defects remain an overarching problem. This work introduces low-temperature chemically self-aligned film growth *via* simultaneous thin film deposition and etching in adjacent regions on a nanopatterned surface. During deposition, nucleation defects are avoided in nongrowth regions because deposition reactants are locally consumed *via* sacrificial etching. For a range of materials and process conditions, thermodynamic modeling confirms that deposition and etching are both energetically favorable. We demonstrate nanoscale patterning of tungsten at 220 °C with simultaneous etching of TiO_2. Area selective deposition (ASD) of the sacrificial TiO_2 layer produces an orthogonal sequence for self-aligned patterning of two materials on one starting pattern, *i.e.*, TiO_2 ASD on SiO_2 followed by W ASD on Si−H. Experiments also show capacity for self-aligned dielectric patterning *via* favorable deposition of AlF_3 on Al_2O_3 at 240 °C with simultaneous atomic layer etching of sacrificial ZnO. Simultaneous deposition and etching provides opportunities for low-temperature bottom-up self-aligned patterning for electronic and other nanoscale systems.

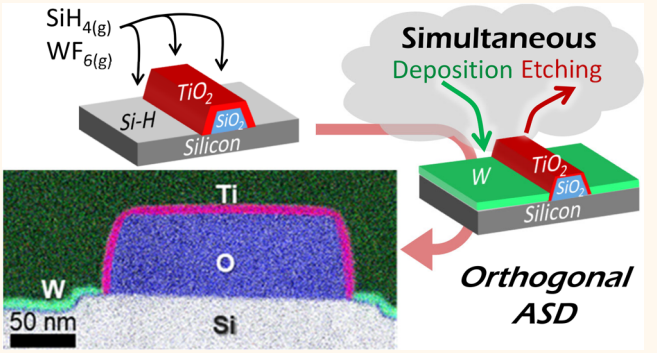

KEYWORDS: *area-selective deposition, etching, patterning, orthogonal, self-aligned*

The smallest printed features in semiconductor manufacturing are currently less than 15 nm.[1] Continued scaling poses significant problems in material patterning and feature alignment.[1−4] Techniques to create small features are well-developed, but a key barrier is the limited ability to control minute variations in feature pattern alignment. Devices are constructed with hundreds of layers of patterned metals and dielectrics, and achieving circuit performance requires the conductors and insulators in each layer to be precisely registered as they form on top of each other. Patterns that are misaligned by only a few nanometers (a distance corresponding to ∼10 atoms in crystalline silicon) can lead to faults including electrical shorts, open circuits, and excess resistance.[4] To avoid metal diffusion, reaction temperature during "back-end" fabrication is limited to <400 °C,[3] putting stringent demands on surface chemical processes. Advanced 13.5 nm extreme UV (EUV) lithography can address some of these challenges, but equipment costs are expected to be substantial,[5] especially when multiple EUV steps are needed. Also, alignment problems will become more acute in future 3D devices being considered to overcome impending obstacles of silicon memory density and computing energy consumption.[1]

To overcome inherent variability and stochastics in lithography, new self-alignment methods are needed where the chemistry of the underlying surface can guide the placement of overlying material layers. Self-aligned area-selective deposition (ASD) uses surface chemistry to promote deposition in predetermined growth regions and minimize growth in adjacent nongrowth regions. At <400 °C, ASD can proceed using chemical vapor deposition (CVD)[3,6−11] or atomic layer deposition (ALD).[12−16] In these methods, the

Received: May 13, 2021
Accepted: June 17, 2021
Published: June 25, 2021

https://doi.org/10.1021/acsnano.1c04086
ACS Nano 2021, 15, 12276−12285

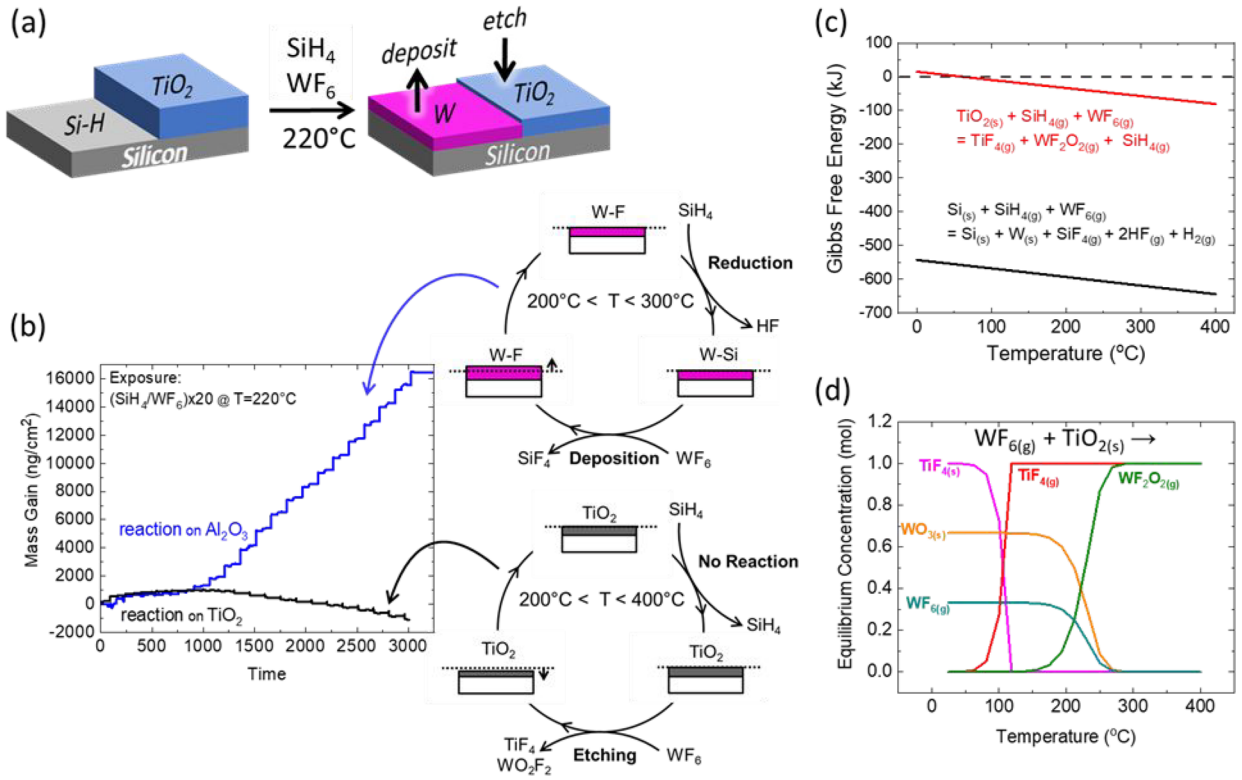

Figure 1. Schematic for self-aligned patterning using simultaneous deposition and etching: (a) starting Si−H/TiO_2 pattern exposed to a set of reactants (in this example, SiH_4/WF_6 in an ALD-type reaction sequence for 20 cycles), yielding W growth on silicon, with no growth in the TiO_2 region due to simultaneous TiO_2 etching. (b) Mass change (ng/cm^2) measured by QCM during SiH_4/WF_6 exposures (SiH_4/Ar/WF_6/Ar = 45/45/1/60 s) at 220 °C, along with the expected reactions during SiH_4 and WF_6 exposure steps on W and on TiO_2 surfaces. The indicated product species are from thermodynamic analysis. A QCM precoated with Al_2O_3 shows net mass gain indicating favorable ALD of W (blue line). On the basis of the density of W, the growth rate is ~0.5 nm/cycle. Under identical conditions, a QCM crystal precoated with TiO_2 shows net mass loss corresponding to etching (black line), with an etch rate of ~0.1 nm/cycle. (c) Overall Gibbs free energy change for SiH_4/WF_6 reactions on TiO_2 (red) and Si (black) surfaces, consistent with the QCM results in panel b. (d) Thermodynamic equilibrium product compositions for WF_6 reacting with an equimolar composition of TiO_2, further supporting simultaneous deposition and etching.

vapor-phase reactants are generally selected to favor net deposition; *i.e.*, the Gibbs free energy change for deposition is negative, $\Delta G < 0$.[17,18] However, the strong reaction energetics is problematic for ASD because it leads to creation of unwanted nucleation defects. Surface passivation layers or other means can slow the rate of nucleation, but unwanted nuclei eventually form, leading to undesired growth and loss of self-alignment. During "front-end" processing, temperatures can exceed 700 °C, and selective silicon epitaxy is widely used to self-align the source/drain contacts to silicon channels. Using high temperatures, defect nuclei are effectively avoided by optimizing reaction thermodynamics.[8−11,19−21] For selective silicon epitaxy, a single set of gas-phase precursors (often including a mixture of chlorosilanes, HCl, and hydrogen) can allow favorable silicon film growth on receptive regions, while, in neighboring regions, the same reactants favor formation of only volatile silicon products, such as $SiCl_2$.[11,20] In this way, self-aligned selective epitaxy avoids defects using thermodynamically favorable reactions that locally consume the deposition reactant in the regions where growth is not desired.

Several vapor/surface exchange and conversion reaction mechanisms are known where material deposition simultaneously liberates another volatile species at the surface deposition site.[22−24] In contrast, low-temperature surface reactions that achieve simultaneous delocalized deposition and etching in neighboring regions on a patterned surface are not well known.

In this work, we demonstrate low-temperature (<400 °C) self-aligned deposition using a single set of vapor-phase reactants to achieve deposition in a desired growth region while simultaneously etching a neighboring sacrificial surface in a nongrowth region. The primary example reported here shows self-limiting ALD with simultaneous continuous chemical vapor etching (CVE), and an alternate example shows ALD with simultaneous self-limiting atomic layer etching (ALE). Akin to high-temperature selective epitaxy reactions, the resulting net deposition is inherently self-aligned with the prepatterned starting surface because the etching reaction locally consumes the deposition reactant, thereby avoiding unwanted nuclei.

Starting with a patterned surface with exposed hydrogen-terminated silicon (Si−H) and TiO_2 regions, we show that sequential exposures of SiH_4 and WF_6 at 220 °C produce self-aligned growth of tungsten only on the silicon, while simultaneously, on the neighboring TiO_2, the WF_6 preferentially reacts to form volatile WO_2F_2 and TiF_4, thereby avoiding tungsten metal growth. At the reaction temperature, the deposition and etching rates are sufficient to avoid accumulation of unwanted W metal until the sacrificial layer is consumed. By creating the starting pattern using area-selective deposition of TiO_2 on SiO_2,[16] we establish a primary

https://doi.org/10.1021/acsnano.1c04086
ACS Nano 2021, 15, 12276−12285

experimental demonstration of multiple-material orthogonal area-selective deposition.[25] Using a combination of thermodynamic modeling and experiments, we further show that self-aligned deposition and etching can be extended to a range of other material systems and show experimental results confirming that deposition of AlF_3 dielectric can proceed with atomic layer etching of ZnO.

RESULTS AND DISCUSSION

The reaction scheme for self-aligned pattern generation using simultaneous deposition and etching is shown in Figure 1a. For this example system, a surface with open Si−H and TiO_2 regions is exposed to multiple cycles of SiH_4/WF_6 co-reactants separated by Ar purge at 220 °C, resulting in W deposition on the Si−H region and simultaneous etching of the sacrificial TiO_2. We performed *in situ* quartz crystal microbalance (QCM) experiments to monitor the surface mass change on two different surfaces exposed to the same reaction conditions, and results are given in Figure 1b. For this study, a QCM crystal was pretreated *in situ* with 25 cycles of Al_2O_3 ALD to create a surface receptive to W growth, similar to QCM crystals coated with silicon.[26] This was followed immediately in the same reactor by 20 cycles of sequential $SiH_4/Ar/WF_6/Ar$ exposures at 220 °C.[27]

The blue line in Figure 1b shows the mass change (ng/cm^2) during the SiH_4/WF_6 cycles, indicating that after a few initial cycles this process gives net atomic layer deposition of tungsten on Al_2O_3. Consistent with previous studies,[26] after ∼5 cycles of growth initiation on Al_2O_3, mass increases linearly with cycles, which on the basis of the density of W correlates to a W growth rate of ∼0.5 nm/cycle. The black line in Figure 1b gives the mass change collected during 20 cycles of $SiH_4/Ar/WF_6/Ar$ under identical reactor conditions, except, for this case, the QCM crystal was prepared by coating with 200 cycles of TiO_2 ALD using $TiCl_4/H_2O$ doses at 220 °C. The results show a small mass gain due to initial uptake of tungsten and fluorine, followed by net mass loss, consistent with TiO_2 etching *via* reaction with WF_6 to form volatile $WF_2O_2(g)$.[28,29] Using the density of TiO_2, the mass change correlates with a loss of ∼2 nm during the 20 cycles, for an average of ∼0.1 nm/cycle.[28,29]

Figure 1b also includes schematics of the reactions corresponding to the QCM results, and panels c and d of Figure 1 show corresponding thermodynamic equilibrium analysis of the expected reactions and reaction products.[30] When SiH_4 and WF_6 react on a receptive growth surface, the net Gibbs free energy change (black line in Figure 1c) shows large $-\Delta G$ values across a wide temperature range. The SiH_4 acts as a reducing agent, with some Si−H remaining on the surface after exposure. The surface Si−H is then available to promote reduction and net deposition during the WF_6 exposure step.[27,31] This produces the stepwise mass uptake observed in the QCM data. On the TiO_2 surface, however, etching reactions become available. In Figure 1c, the red line shows the overall Gibbs free energy change when SiH_4 and WF_6 react with TiO_2. For temperatures above 75 °C, a favorable reaction ($\Delta G < 0$) yields volatile TiF_4 and WF_2O_2, with no net reaction for the SiH_4. Because SiH_4 does not react on TiO_2 at low temperature, surface Si−H groups are not available to reduce the WF_6, thereby promoting WF_6 to react and be consumed by the etch reaction. Likewise, Figure 1d gives the expected equilibrium product concentrations when WF_6 reacts with TiO_2 at different temperatures. At 220 °C, the expected products are TiF_4 and WF_2O_2 vapors. Some tungsten oxide solid may also be expected, but oxide buildup is avoided due to continued formation of $WF_2O_2(g)$ as a volatile etch product.[28,29] For the SiH_4/WF_6 reaction on TiO_2, the QCM results in Figure 1b are consistent with negligible reaction during SiH_4 and net mass loss during the WF_6 dose. XPS surface analysis results in Supporting Information Figure S1 further confirm minimal reaction with SiH_4.

We also used ellipsometry and XPS to analyze simultaneous deposition and etching reactions during SiH_4/WF_6 exposure on Si−H and TiO_2 surfaces. On patterned wafers discussed below, Si−H and TiO_2 surfaces are formed by applying TiO_2 ASD to $Si-H/SiO_2$ patterns. This is followed by W ASD, producing a multiple-material orthogonal ASD sequence[25] (*i.e.*, TiO_2 ASD on SiO_2 followed by W ASD on Si−H). Therefore, for ellipsometry and XPS analysis, the starting Si−H and TiO_2 samples also were prepared by TiO_2 ASD, following the same procedure used below for $Si-H/TiO_2$-patterned wafers. Specifically, a pair of silicon wafer pieces, one with silicon oxide (Si−OH) and one with Si−H termination, were simultaneously exposed to TiO_2 ASD at 150 °C using a "supercycle" sequence, including TiO_2 ALD cycles with periodic atomic layer etching steps.[16] This was followed by a 5 s dip in dilute (5%) HF solution and immediate transfer to the SiH_4/WF_6 reactor. The intermediate HF dip step facilitated the desired W nucleation on Si−H and removed ∼5 nm of the deposited TiO_2 layer (Figure S2 and Table S2). The procedure was also tested without any intermediate treatment and with intermediate H_2/Ar plasma exposure. As discussed in the Supporting Information, samples without HF treatment or with H_2/Ar plasma exposure showed an unfavorable delay in W growth on the Si−H. Therefore, the HF dip was used for further analysis.

After TiO_2 ASD on Si−OH and Si−H, ellipsometry data (Table S2) shows TiO_2 thickness of 16.4 nm on the Si−OH and ∼1.9 nm on the Si−H. After HF, ellipsometry showed no oxide on Si−H, with 11.4 nm of TiO_2 on the Si−OH, indicating a loss of ∼5 nm of TiO_2. After simultaneous exposure to 15 cycles of SiH_4/WF_6 at 220 °C, the Si−H sample showed a net growth of 9.7 nm of W, while the TiO_2 film showed a net thickness decrease of ∼1.1 nm. Using newly prepared Si−H and TiO_2 samples, the experiment was repeated using 20 cycles of SiH_4/WF_6. On Si−H, 20 SiH_4/WF_6 cycles produced 12.6 nm of W, with a net TiO_2 thickness decrease of ∼1.4 nm.

The measured thickness change indicates the SiH_4/WF_6 allowed simultaneous deposition and etching, consistent with QCM in Figure 1. From the thickness data, the W deposition rate is ∼0.6 nm/cycle and the etch rate of the TiO_2 is ∼0.1 nm per ALD cycle, in reasonable agreement with the deposition rate of ∼0.5 nm/cycle and etch rate of ∼0.1 nm/cycle estimated from the QCM results in Figure 1b. Under the conditions used, this etching rate is sufficient to avoid W growth.

For this approach to be useful, it should be compatible with different methods to form patterned sacrificial materials. A possible issue is that the rate of etching will depend on the process used to form the sacrificial layer. For example, using TiO_2 deposited by physical vapor deposition, initial experiments show a slower etch rate. The slower etching consumes less reactant, and therefore promotes unwanted deposition. To address this, the process provides flexibility to allow tuning of the relative deposition and etching rates. For the W/TiO_2

https://doi.org/10.1021/acsnano.1c04086
ACS Nano 2021, 15, 12276−12285

Table 1. XPS Atomic Fraction (at. %) Measured on Si−H and TiO_2 before and after Exposure to 15 or 20 Cycles of SiH_4/WF_6 at 220 °C[a]

		XPS atomic fraction (at. %)							
surface	SiH_4/WF_6 treatment at 220 °C	Ti 2p	W 4d	Si 2p	O 1s	F 1s	Cl 2p	B 1s	C 1s
Si−H	none	0	0	79.2	7.5	1.2	0	0	12.1
	15 cycles	0	20.2	1.5	53.7	0.3	0	0	24.3
	20 cycles	0	22.2	2.6	47.4	0	0	0	27.8
TiO_2	none	18.0	0.4	0	48.5	6.8	0.7	4.9	20.7
	15 cycles	17.7	4.1	0.2	55	2.1	0.4	3	17.5
	20 cycles	15.1	2.5	1.6	52	1.3	0	2.5	25

[a]The starting Si−H and TiO_2 were prepared by exposing Si−H or Si−OH wafers to TiO_2 ALD/ALE supercycles,[16] following the same procedure applied to Si−H/SiO_2-patterned wafers discussed in the text.

system, increasing substrate temperature from 220 to 275 °C does not substantially change the W deposition rate,[27] but a larger etching rate is observed (Table S3), thereby allowing process adjustment and optimization.

The same blanket samples used for thickness measurement were also analyzed by XPS to evaluate the surface element composition after SiH_4/WF_6 treatment, and results are shown in Table 1. As expected, all samples show oxygen and carbon resulting from exposure to the ambient between deposition and analysis. On the Si−H surface, both 15 and 20 SiH_4/WF_6 cycles lead to strong W signals, consistent with expected W deposition on the receptive Si−H. Also as expected, the signal from Ti 2p was below the detection limit (<0.1 at. %). A small Si signal after SiH_4/WF_6 is ascribed to remnant surface silicon from the silane reducing agent. On the TiO_2 surface, the SiH_4/WF_6 leads to a small amount of W (~2.5−4.1 at. %), ascribed to formation of tungsten oxides, as expected from the thermodynamic analysis shown in Figure 1d.[29] We also note that the amount of W on TiO_2 does not increase when the number of W ALD cycles increases from 15 to 20, further indicating that tungsten oxide does not accumulate on the TiO_2.[28,29] This small amount of tungsten oxide on the TiO_2 can be effectively removed by exposing the surface to BCl_3 vapor at the reaction temperature (Table S4).

We applied this approach on microscale and nanoscale line/space patterns. Microscale-patterned substrates, used previously for ASD studies,[16,31,32] consisted of 3 μm wide SiO_2 lines, ~100 nm thick, separated by 3 μm of exposed Si−H (*i.e.*, 6 μm full-pitch). To form the patterned sacrificial TiO_2 layers, Si−H/SiO_2 samples were coated at 150 °C by ASD TiO_2 using a supercycle sequence as mentioned above. A sequence of 20 supercycles produced ~16.4 nm of TiO_2 atop the SiO_2 regions, with minimal TiO_2 on adjacent Si−H regions.[16] After TiO_2 ASD, samples were treated with a 5 s dip in dilute (5%) HF solution and immediately transferred to the SiH_4/WF_6 reactor to perform the second ASD step using simultaneous W deposition and TiO_2 etching. This sequence of TiO_2 ASD on SiO_2 followed by W ASD on Si−H provides an experimental demonstration of multiple-material orthogonal ASD.[25]

The resulting microscale self-aligned W/TiO_2 patterns are shown in Figures 2 and 3. Figure 2b shows cross-sectional scanning transmission electron microscopy (STEM) images and corresponding STEM-EDX (EDX, energy-dispersive X-ray spectroscopy) data after treating the TiO_2/Si−H pattern with 15 cycles of SiH_4/WF_6 at 220 °C. A tungsten film with thickness of 7.0 ± 0.4 nm (given as the mean of 8 measurements ± 1 standard deviation) is visible only on the Si−H region, and the TiO_2 is visible only atop the SiO_2. The remaining ASD TiO_2 layer is 4.9 ± 0.3 nm thick, indicating

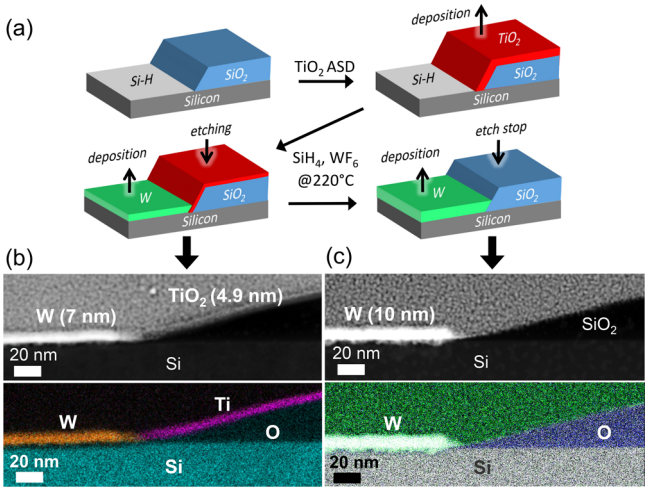

Figure 2. Self-aligned orthogonal microscale patterning of TiO_2 and W films: (a) Schematic sequence used for preparation of patterned sacrificial TiO_2 layer, followed by simultaneous deposition and etching to form the self-aligned W and TiO_2. (b) Cross-sectional STEM and STEM-EDX after 15 SiH_4/WF_6 cycles. (c) Data collected from an identical sample after 20 SiH_4/WF_6 cycles. The images show the SiH_4/WF_6 cycles produce net W deposition in exposed Si−H regions, with simultaneous etching of the sacrificial TiO_2 layer.

that the HF dip + SiH_4/WF_6 treatment removed ~11 nm of TiO_2. The experiment was repeated on another TiO_2/Si−H substrate with ~16.4 nm of ASD TiO_2, except for the second ASD step; the SiH_4/WF_6 exposure was performed for 20 cycles. Figure 2c shows the resulting STEM and STEM-EDX images. In this case, the samples show 10.0 ± 0.6 nm of W on Si−H, with no visible TiO_2 on the SiO_2. The 20 W ALD cycles were sufficient to completely remove the sacrificial TiO_2, while simultaneously depositing 10 nm of W in the neighboring Si−H regions.

Comparing the thicknesses of the TiO_2 and W films in Figure 2 to those measured by ellipsometry on blanket substrates following identical process conditions, the patterned wafers show somewhat thinner W layers. The patterned wafers also show net thinner TiO_2 layers compared to the blanket samples. This thinner TiO_2 layer may result from faster etching on the patterned surface. Mechanisms leading to pattern-dependent deposition and etching rates are well-known during ASD[3,9,31,33] and generally relate to gas-transport and surface diffusion effects that alter the local reactant concentration and supersaturation across the sample surface. As discussed below,

https://doi.org/10.1021/acsnano.1c04086
ACS Nano 2021, 15, 12276−12285

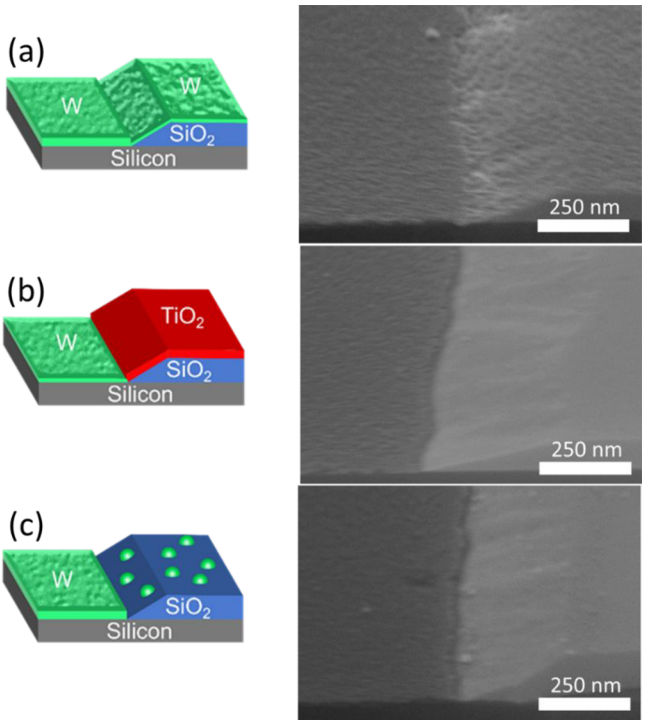

Figure 3. Angled-view SEM for (a) Si−H/SiO_2 patterns with no TiO_2 present after 20 cycles of SiH_4/WF_6, indicating W deposition on both of Si−H and SiO_2; (b) the sample from Figure 2b, showing surface texture consistent with W deposition on Si−H and simultaneous etching of the TiO_2; and (c) the sample from Figure 2c showing a small number of W nuclei on SiO_2, consistent with consumption of the TiO_2 sacrificial layer.

understanding pattern-dependent reaction rates remains an overarching issue for self-aligned deposition-based patterning.

The self-aligned patterned samples shown in Figure 2 were also analyzed by angled-view SEM, and images are presented in Figure 3. Figure 3a shows a control Si−H/SiO_2 wafer (with no TiO_2 initially present) treated with 20 cycles of SiH_4/WF_6. The SiH_4/WF_6 produces a cohesive W film on Si−H, and the rough texture on SiO_2 is consistent with W nuclei.[31] Figure 3b shows the sample from Figure 2b, corresponding to Si−H/TiO_2 after 15 cycles of SiH_4/WF_6. Both the TiO_2 and W regions appear smooth, with no visible W nuclei on the TiO_2. Figure 3c shows the sample from Figure 2c, identical except after 20 SiH_4/WF_6 cycles. Some particles appear in the SiO_2 region likely corresponding to W nuclei that are expected to form after complete consumption of the TiO_2. Similarly sized nuclei (10−20 nm) formed during ASD were previously analyzed using SEM-EDX, but sensitivity was limited by the small volume of the nuclei.[16]

We further confirmed that the approach could extend to nanoscaled patterns, and results are given in Figure 4. The figure includes a schematic diagram, along with corresponding STEM and STEM-EDX images of self-aligned W and TiO_2 on ~200 nm of Si−H/SiO_2-patterned substrates (~400 nm full-pitch) using the same condition as for samples in Figure 2b. Four neighboring features in Figure 4b show consistent pattern duplication, with an expanded higher resolution view of one example region in Figure 4c,d. The sequence yielded 6.1 ± 0.5 nm of W on the Si−H region and 5.8 ± 0.3 nm of TiO_2 on the SiO_2. These values are reasonably similar to those in Figure 2b obtained on the 3 μm features.

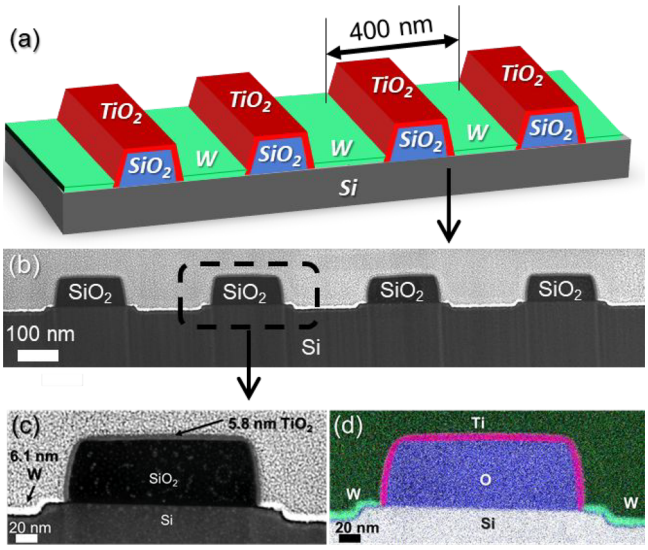

Figure 4. (a) Broad-view schematic of the orthogonal selective deposition of W and TiO_2 on Si−H/SiO_2-patterned surfaces (200 nm width and ~100 nm height) after TiO_2 20 supercycles and W 15 cycles. (b) Cross-sectional STEM of the multiple patterns: (c) zoom-in view of one pattern from panel b; (d) STEM-EDX corresponding to image panel c.

Careful inspection of the high-resolution images shows that the TiO_2 layer may be thinner on top of the corner edge of the SiO_2, possibly indicating faster TiO_2 etching on exposed corners. The high-resolution images also show uniform W thickness on the exposed silicon, with no visible W nuclei on the TiO_2. The TiO_2/W feature edge boundaries appear well-defined, but understanding feature development at the atomic scale remains a challenge. Figure S3 shows additional TEM/STEM images of self-aligned nanopatterned W/TiO_2 samples.

This work presents simultaneous deposition and etching as a route for direct-patterned area-selective deposition. Also importantly, as shown in Figures 2 and 4, we show that the starting sacrificial pattern can be formed by area-selective deposition, thereby confirming experimental feasibility for orthogonal multiple-material patterning[25] as a step forward in bottom-up nanomaterial surface synthesis.

Extension to Other Material Systems. In addition to the W/TiO_2 system, thermodynamic modeling[30] and published rate data indicate that simultaneous deposition and etching can be achieved for a range of other deposition and sacrificial materials. Examples are presented in Table 2. The table include calculated values of the Gibbs free energy changes for atomic layer deposition and etching and the approximate overlapping temperature range, where both reactions are expected to be energetically favorable. Where available, the table also includes experimental values for atomic layer deposition and etching rates at an example temperature within the favorable temperature range. For some systems, a range of etch rates is reported because etch kinetics can depend strongly on detailed process conditions. The etching rates (nm/cycle) correspond to the expected thickness loss during the simultaneous atomic layer deposition cycle. We further note that, for some materials sets, reaction thermodynamics may favor simultaneous deposition and etching but slow reaction kinetics may make them experimentally difficult. The deposition reactions are expected to proceed on any receptive surface where etching does not occur.

https://doi.org/10.1021/acsnano.1c04086
ACS Nano 2021, 15, 12276−12285

Table 2. Partial List of Example Material Systems Showing Thermodynamic Feasibility for Self-Aligned Patterning *via* Simultaneous Deposition and Etching[a]

ASD material	Sacrificial material	Reactants	T range (°C)		Expected reactions	Example T (°C)	Rate (nm/cycle)	ΔG (kJ/mol) @ example T	Reference
W	TiO_2	SiH_4, WF_6	200 - 300	Deposition	$SiH_4 + WF_6 \rightarrow W_{(s)} + SiF_{4(g)} + HF_{(g)} + H_{2(g)}$	220	0.58	-598	this work, 27
				Etching	$TiO_2 + SiH_4 + WF_6 \rightarrow TiF_{4(g)} + WO_2F_{2(g)} + SiH_{4(g)}$		0.02 - 0.2	-38	this work, 29
WO_3	TiO_2	SiH_4, WF_6, H_2O	200 - 275	Deposition	$WF_{6(g)} + SiH_{4(g)} + 3H_2O_{(g)} \rightarrow WO_{3(s)} + SiF_{4(g)} + 2HF_{(g)} + 4H_{2(g)}$	220	0.58	-653	27, 36
				Etching	$TiO_{2(s)} + SiH_{4(g)} + WF_{6(g)} + H_2O_{(g)} \rightarrow TiF_{4(g)} + WO_2F_{2(g)} + SiH_{4(g)} + H_2O_{(g)}$		0.02 - 0.2	-38	this work, 29
WO_3	TiN	H_2O, SiH_4, WF_6	200 - 275	Deposition	$WF_{6(g)} + SiH_{4(g)} + 3H_2O_{(g)} \rightarrow WO_{3(s)} + SiF_{4(g)} + 2HF_{(g)} + 4H_{2(g)}$	220	0.58	-653	27, 36
				Etching	$TiN_{(s)} + 2H_2O_{(g)} + SiH_{4(g)} + WF_{6(g)} \rightarrow TiF_{4(g)} + WO_2F_{2(g)} + SiH_{4(g)} + NH_{3(g)} + 0.5H_{2(g)}$		0.02 - 0.2	-158	this work, 29
WS_2	TiO_2	WF_6, H_2S	250 - 300	Deposition	$H_2S + WF_6 \rightarrow WS_{2(s)} + HF_{(g)} + S_{2(g)}$	300	~0.1	-409	37
				Etching	$TiO_2 + WF_6 + H_2S \rightarrow TiF_{4(g)} + WO_2F_{2(g)} + H_2S_{(g)}$		~0.3	-57	29
AlF_3	ZnO	HF, TMA	200 - 250	Deposition	$Al(CH_3)_{3(g)} + 3HF_{(g)} \rightarrow AlF_{3(s)} + 3CH_{4(g)}$	220	~0.05	-701	34
				Etching	$ZnO_{(s)} + 2HF_{(g)} + 2Al(CH_3)_{3(g)} \rightarrow Zn(CH_3)_{2(g)} + 2AlF(CH_3)_{2(g)} + H_2O_{(g)}$		0.11	< 0[b]	35
AlF_3	Ga_2O_3	HF, TMA	200 - 250	Deposition	$Al(CH_3)_{3(g)} + 3HF_{(g)} \rightarrow AlF_{3(s)} + 3CH_{4(g)}$	250	~0.05	-699	34
				Etching	$Ga_2O_{3(s)} + 6HF_{(g)} + 4Al(CH_3)_{3(g)} \rightarrow 3H_2O_{(g)} + 2GaF(CH_3)_{2(g)} + 4AlF(CH_3)_{2(g)}$		~0.082	< 0[b]	38
Si_3N_4	HfO_2	HF, $SiCl_4$, NH_3	300 - 350	Deposition	$3SiCl_{4(g)} + 4NH_{3(g)} \rightarrow Si_3N_{4(s)} + 12HCl_{(g)}$	350	0.2	-104	39
				Etching	$HfO_{2(s)} + 4HF_{(g)} + SiCl_{4(g)} \rightarrow 2H_2O_{(g)} + SiF_{4(g)} + HfCl_{4(g)}$		0.005	-77	40
SnS	HfO_2	HF, $Sn(acac)_2$, H_2S	200 - 250	Deposition	$Sn(acac)_{2(g)} + H_2S_{(g)} \rightarrow SnS_{(s)} + 2H(acac)_{(g)}$	200	0.019	< 0[b]	41
				Etching	$HfO_{2(s)} + 4HF_{(g)} + 4Sn(acac)_{2(g)} \rightarrow Hf(acac)_{4(g)} + 4SnF(acac)_{(g)} + 2H_2O_{(g)}$		0.006	< 0[b]	40
SnS	Al_2O_3	HF, $Sn(acac)_2$, H_2S	200 - 250	Deposition	$Sn(acac)_{2(g)} + H_2S_{(g)} \rightarrow SnS_{(s)} + 2H(acac)_{(g)}$	200	0.019	< 0[b]	41
				Etching	$Al_2O_{3(s)} + HF_{(g)} + Sn(acac)_{2(g)} \rightarrow Al(acac)_{3(g)} + SnF(acac)_{(g)} + H_2O_{(g)}$		0.023	< 0[b]	40

[a]The reported temperature range indicates the values where simultaneous deposition and etching are expected to both be energetically favorable. The reported Δ*G* values for deposition and etching are evaluated at the example temperature shown. Rates are estimated from published reports of deposition by ALD and etching by CVE or ALE determined from ellipsometry. Etch rates correspond to the expected amount etched per ALD cycle. [b]Favorable reaction energetics consistent with published experimental results.

As one example, data in Table 2 indicate that, with use of trimethylaluminum (TMA) and hydrogen fluoride (HF) as co-reactants at 240 °C, a receptive surface (such as Al_2O_3)[34] is expected to yield favorable deposition of AlF_3. Further, when a ZnO surface is exposed to these same conditions, reaction energetics favors ZnO atomic layer etching, producing volatile dimethyl zinc, dimethyl aluminum fluoride, and water.[35]

To confirm the feasibility of the AlF_3 and ZnO system, we used QCM analysis to observe mass changes on different surfaces exposed to HF/TMA and results are shown in Figure 5. For these data, the experimental procedure follows that was used to collect data in Figure 1. First, a QCM crystal was precoated with ALD Al_2O_3 at 150 °C to be receptive to AlF_3, followed by exposure to repeated doses of HF and TMA at 240 °C. The data in Figure 5 show stepwise mass gain, consistent with ALD of AlF_3.[34] Also in Figure 5, a second QCM crystal was precoated with ZnO at 150 °C and then exposed to HF/TMA under identical conditions at 240 °C. The QCM results show clear mass loss, consistent with ZnO etching.[35] Therefore, the concept demonstrated above for simultaneous deposition and etching can also be extended to other ASD material systems, including AlF_3 on Al_2O_3 with sacrificial etching of neighboring ZnO.

CONCLUSIONS

In summary, our findings highlight the importance of thermodynamically designed surface chemistry for nanoscale self-aligned thin film patterning. Counterintuitively, results show that, at low temperatures, using a single set of reactants, it is possible for both deposition and etching to be favored at the same time on different regions of an exposed patterned surface. This means that unwanted nucleation, a broad problem in area-selective deposition, can be avoided because the etching reaction locally consumes the nucleation reactants. This approach to avoid unwanted nucleation may be useful for low-temperature self-aligned patterning in back-end electronics manufacturing and other nanoscale material systems. As one key prospect, we show a sequence of two deposition processes can orthogonally self-align two different materials in different regions on a single starting patterned substrate.

https://doi.org/10.1021/acsnano.1c04086
ACS Nano 2021, 15, 12276−12285

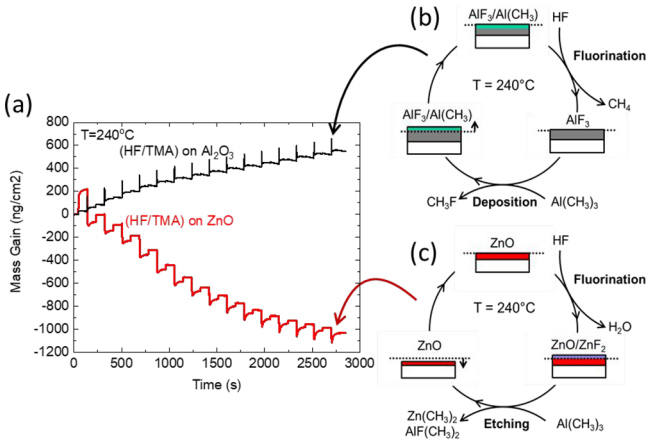

Figure 5. (a) Collected QCM mass gain data from Al_2O_3 or ZnO precoated crystals during 15 cycles of (HF/TMA) exposures. (b) AlF_3 deposition mechanism on Al_2O_3 surface and (c) ZnO atomic layer etching mechanism on ZnO during 15 HF/TMA cycles. Reaction schemes indicate the expected dominant products from thermodynamic analysis.

Our findings also reveal several challenges and remaining problems. One challenge is that reaction conditions should allow the etching and deposition rates to be balanced so that the etching rate is sufficient to consume the gas-phase reactants and avoid unwanted nucleation, with fast enough deposition to develop the desired pattern thickness. Also, while we show the approach works using tungsten and TiO_2, which are important materials in semiconductor processing, semiconductor device manufacturers are seeking self-aligned patterning solutions for a broad and expanding set of materials. Discovering additional material systems will require more extensive modeling and may include the design of new precursors and reactants. Another important outstanding problem is to what extent this process can apply to features approaching atomic scale dimensions. Results show uniform patterning at the 200 nm scale, but we see that etching and deposition rates may depend on feature shape and size. Further scaling will require better understanding of these effects.

Eventually, scaling of deposition-based self-aligned patterning to single-atom dimensions will allow ultimate precision in materials fabrication. Achieving this feat using designed surface chemistry will be a critical step toward producing large numbers of devices in parallel across large surface areas under conditions using limited thermal exposure.

METHODS

Substrate Preparation. For all deposition studies reported here, each run was performed using wafer pieces with Si−H/SiO_2 patterns and/or separate blanket Si−H and Si−OH pieces, with both pieces always present in the deposition chamber. Surfaces designated as "Si−OH" consist of piranha cleaned silicon producing hydroxyl termination, whereas surfaces designated as "SiO_2" are thermally oxidized silicon, also with hydroxyl termination. "Si−H" surfaces are formed by dipping the Si−OH in 5% HF for 30 s, producing hydrogen termination. Before deposition, lithographically patterned Si−H/SiO_2 substrates were prepared by piranha cleaning and HF dipping of Si/SiO_2. The piranha solution was prepared by mixing 30% hydrogen peroxide (electronic grade, J.T. Baker) and 98% sulfuric acid (certified ACS plus, Fisher Chemical) with 1:1 volume ratio.

A boron-doped silicon (100) wafer with 5−10 Ω·cm resistivity was cleaved into small pieces (10 mm × 10 mm). These wafer pieces were cleaned with the piranha solution for 15 min, rinsed with deionized (DI) water, and stored in a DI water filled glass vial. They served as our oxide-terminated blanket silicon substrates (Si−OH) after being rinsed with DI water and dried with N_2 flow.

Hydrogen-terminated blanket silicon (Si−H) samples were prepared from the Si−OH pieces described above by employing a 30 s dip in 5% HF solution, a 30 s rinse in flowing DI water, and then drying with N_2. The Si−H substrates were always loaded into the reactor within 10 min after preparation.

Si/SiO_2 line patterned substrates were prepared by photolithographic wet etching of 100 nm thick thermally grown silicon dioxide (SiO_2) on silicon wafers. The pattern consists of long (>10 mm) alternating lines of SiO_2 and Si, each 3 μm wide for a 6 μm pitch. The wafer was cleaved into small pieces (10 mm × 10 mm) and prepared immediately prior to loading, as described above for Si−H sample preparation. The 200 nm half-pitch patterned samples were provided by industry and prepared in the same way.

TiO_2 ALD/ALE Supercycles Condition. TiO_2 ALD was performed using 99% pure $TiCl_4$ (Strem Chemicals) and deionized water (DI water), and the ALE was performed using 99.999% pure WF_6 (Galaxy Chemicals) and 99.9% pure BCl_3 (Matheson). The ALD/ALE supercycles were conducted in a custom-built tubular hot-walled isothermal viscous-flow ALD reactor, further notified as "TiO_2 reactor", under constant wall temperature (150 °C) and pressure (0.9−1.1 Torr) with 150 sccm of 99.999% pure N_2 (Arc3 Gases) as a carrier gas. One TiO_2 ALD cycle was defined as "$TiCl_4$ pulse (0.1 s) → N_2 purge (45 s) → H_2O pulse (0.05 s) → N_2 purge (45 s)" and one TiO_2 ALE cycle was defined as "WF_6 pulse (0.1 s) → N_2 purge (45 s) → BCl_3 pulse (1 s) → N_2 purge (45 s)". One TiO_2 ALD/ALE supercycle consisted of 30 cycles of $TiCl_4/H_2O$ (for TiO_2 ALD) followed by 7 cycles of WF_6/BCl_3 (TiO_2 ALE). The supercycles were performed in a single reactor at a fixed temperature of 150 °C. Using 12 or 20 supercycles produced ∼11.5 and ∼16.4 nm of TiO_2 on Si−OH, respectively, with less than 1.9 nm of TiO_2 on exposed Si−H surfaces.

W ALD Cycles Condition. W ALD, using 2% SiH_4 (Custom Gas Solution) and 99.999% pure WF_6 (Galaxy Chemicals), was performed in a separate custom-built tubular hot-walled isothermal viscous-flow ALD reactor, further notified as "W reactor", under constant wall temperature (220 °C) and pressure (2.0−2.4 Torr) with 210 sccm of 99.999% pure Ar (Arc3 gases) as a carrier gas. One W ALD cycle was define as "SiH_4 pulse (45 s) → Ar purge (45 s) → WF_6 pulse (1 s) → Ar purge (45 s)". W film was deposited on prepared substrates by running W ALD 10−20 cycles. In this experiment, we first performed Al_2O_3 ALD to initialize the internal surface of the hot-walled reactor and the surface of the QCM crystal. Trimethylaluminum (TMA; 98%, Strem Chemicals) and DI water were used for the Al_2O_3 ALD to initialize the wall condition of the W reactor between batches. One cycle of TMA/H_2O was defined as "TMA pulse (0.1 s) → Ar purge (45 s) → H_2O pulse (0.1 s) → Ar purge (45 s)", and 25 cycles of TMA/H_2O were used for the initialization.

Integrated Sequence of "TiO_2 ALD/ALE → HF Dipping → W ALD". Prepared blanket Si−OH and Si−H samples as well as Si−H/SiO_2-patterned substrates were loaded into the TiO_2 reactor and allowed to reach thermal equilibrium for 60 min under 150 sccm of N_2 flow at 150 °C wall temperature. TiO_2 ALD/ALE 12 or 20 supercycles were performed for TiO_2 ASD on SiO_2. Following TiO_2 ASD, the samples were removed from the reactor, dipped into 5% HF for 5 s, rinsed with flowing DI H_2O for 30 s, and dried with N_2 flow in atmospheric conditions to remove undesired oxides on Si−H surfaces. Next, the samples were loaded into the W reactor and allowed to reach thermal equilibrium for 30 min with 210 sccm of Ar flow at 220 °C wall temperature. Subsequently, 10−20 W ALD cycles were carried out at 220 °C to selectively deposit W film on Si−H.

HF/TMA Exposures on ZnO and Al_2O_3. Hydrogen fluoride pyridine (∼70% HF + ∼30% pyridine, Sigma-Aldrich) was used as the HF source. One cycle of HF/TMA exposure was defined as "HF pulse (2 s) → N_2 purge (90 s) → TMA pulse (1 s) → N_2 purge (90 s)", and 15 cycles of HF/TMA exposure were performed at 240 °C after either ZnO or Al_2O_3 predeposition on QCM crystals at 150 °C.

https://doi.org/10.1021/acsnano.1c04086
ACS Nano 2021, 15, 12276−12285

95% pure diethylzinc (DEZ) from Strem Chemicals and DI water were used to deposit ZnO films on QCM crystals. One cycle of DEZ/H_2O was defined as "DEZ pulse (0.5 s) → N_2 purge (60 s) → H_2O pulse (0.1 s) → N_2 purge (60 s)", and 100 cycles of DEZ/H_2O exposure at 150 °C were performed before the HF/TMA exposures at 240 °C.

One cycle of TMA/H_2O was defined as "TMA pulse (0.5 s) → N_2 purge (60 s) → H_2O pulse (0.1 s) → N_2 purge (60 s)", and 100 cycles of TMA/H_2O exposure at 150 °C were performed before the HF/TMA exposures at 240 °C.

Characterization. For monitoring mass uptake on TiO_2 or W films during deposition, a quartz crystal microbalance probe (Kurt Lesker) with a 6 MHz gold-coated crystal sensor (Inficon) was inserted into the reactor and kept in the reactor at least 120 min to be thermally stabilized. To avoid deposition on the exposed electrical contacts, the backside of the crystal was purged with 25 sccm of carrier gas flow during the measurement. *In situ* mass loading (ng/cm^2) was obtained by electronic data acquisition.

W or TiO_2 thickness was measured by *ex situ* spectroscopic ellipsometry (alpha-SE ellipsomter, J.A. Woollam) in the 380−890 nm of wavelength (λ) at 70° incident angle. A Cauchy model provided from J.A. Woollam was used to calculate the TiO_2 thickness. The values for W thickness were estimated by correlating ellipsometry parameters Δ and Ψ collected at λ = 700 nm to film thickness.[31]

Chemical composition of obtained TiO_2 and W films was characterized using *ex situ* X-ray photoelectron spectroscopy (XPS, Kratos Analytical Axis Ultra) with an Al Kα (1486.6 eV) gun (operating at 15 kV and 10 mA). A neutralizer was used to reduce the charging effect. Survey and high-resolution scans were carried out for C 1s, O 1s, F 1s, Cl 2p, Ti 2p, W 4f, W 4d, B 1s, and Si 2p. Casa XPS software was used to process the collected raw data, and peak positions were calibrated with the adventitious C 1s peak as 284.8 eV. The high-resolution and survey scans were used to obtain atomic concentrations (at. %).

Angled- and top-view images of patterned samples were obtained using field emission scanning electron microscopy (SEM, FEI Verios 460L). A high-current Ga^+ liquid metal focused ion beam (FIB; FEI Quanta 3D FEG) was used to prepare samples for TEM. The dual beam FIB provided 7 nm resolution at 30 keV for the ion column and 1.2 nm resolution at 30 keV for the SEM column. Prior to the lift-out, samples were coated with a Pt capping layer with thickness of ∼3.2 μm. The Ga^+ ion source was used to mill-out a 20 μm × 2 μm region, followed by a final milling to ∼100 nm thickness using of 5 kV at 48 pA ion emission current. The TEM specimen was then removed from the sample using a micromanipulator and placed directly onto a 3 mm diameter Cu TEM grid. Cross-sectional images of patterned samples were collected by transmission electron microscopy (TEM; FEI Talos F200X) operated at 200 kV with 0.12 nm resolution. The TEM camera (ThermoFisher Ceta) acquired images with 4*k* × 4*k* resolution. Energy-dispersive X-ray spectroscopy element mapping was performed using scanning transmission electron microscopy (STEM). In STEM mode, the HAADF images were acquired with camera length of ∼100 mm. The FEI Talos F200X TEM uses the Super-X EDX system, which is comprised of four in-column EDX detectors with a collection angle of ∼0.9 sr. The typical parameters for STEM-EDX used a beam current of 350 pA, and each EDX collection time exceeded 5 min.

ASSOCIATED CONTENT

Supporting Information

The Supporting Information is available free of charge at https://pubs.acs.org/doi/10.1021/acsnano.1c04086.

More detailed data, including results of XPS analysis, effect of temperature on TiO_2 etching, and additional TEM/STEM images, as well as discussion and results of intermediate treatments between TiO_2 ASD and W ASD (PDF)

AUTHOR INFORMATION

Corresponding Author

Gregory N. Parsons − *Department of Chemical and Biomolecular Engineering, North Carolina State University, Raleigh, North Carolina 27695, United States;* orcid.org/0000-0002-0048-5859; Email: gnp@ncsu.edu

Authors

Seung Keun Song − *Department of Chemical and Biomolecular Engineering, North Carolina State University, Raleigh, North Carolina 27695, United States;* orcid.org/0000-0002-2214-449X

Jung-Sik Kim − *Department of Chemical and Biomolecular Engineering, North Carolina State University, Raleigh, North Carolina 27695, United States;* orcid.org/0000-0002-3846-4092

Hannah R. M. Margavio − *Department of Chemical and Biomolecular Engineering, North Carolina State University, Raleigh, North Carolina 27695, United States;* orcid.org/0000-0001-5327-3713

Complete contact information is available at: https://pubs.acs.org/10.1021/acsnano.1c04086

Author Contributions

All authors contributed to the reaction modeling, data analysis and interpretation. S.K.S. and J.-S.K. developed and conducted experiments under the supervision of G.N.P. S.K.S., J.-S.K., and H.R.M.M. prepared the draft manuscript, and the text was finalized by G.N.P. S.K.S. and J.-S.K. contributed equally to the project. All authors have given approval to the final version of the manuscript.

Notes

The authors declare no competing financial interest.

Data and Materials Availability: All data needed to evaluate the conclusions in the article are supplied in the manuscript and in associated online content. Additional data may be requested from the authors.

ACKNOWLEDGMENTS

This work was supported by funding from the Semiconductor Research Corporation, Task 2729.001 and Task 3036.001, and from the U.S. National Science Foundation, Award No. 1704151. We thank IBM for supplying wafers with 200 nm half-pitch features. TEM/STEM and SEM were performed at North Carolina State University Analytical Instrumentation Facility (AIF), supported by the state of North Carolina and the National Science Foundation (Award No. ECCS-2025064). XPS was conducted at Duke University Shared Materials Instrumentation Facility (SMIF) and University of North Carolina Chapel Hill Analytical and Nanofabrication Laboratory (CHANL). NNF, SMIF, and CHANL are members of the North Carolina Research Triangle Nanotechnology Network (RTNN), which is supported by the National Science Foundation (Grant ECCS-1542015) as part of the National Nanotechnology Coordinated Infrastructure (NNCI).

REFERENCES

(1) *Decadal Plan for Semiconductors*; Semiconductor Industry Association, Semiconductor Research Corp., 2021. www.src.org/decadal-plan (accessed 2021-06-16).

(2) Clark, R.; Tapily, K.; Yu, K.-H.; Hakamata, T.; Consiglio, S.; O'Meara, D.; Wajda, C.; Smith, J.; Leusink, G. Perspective: New

Process Technologies Required for Future Devices and Scaling. *APL Mater.* **2018**, *6*, 058203.
(3) Parsons, G. N.; Clark, R. D. Area-Selective Deposition: Fundamentals, Applications, and Future Outlook. *Chem. Mater.* **2020**, *32*, 4920−4953.
(4) Mohanty, N.; Smith, J. T.; Huli, L.; Pereira, C.; Raley, A.; Kal, S.; Fonseca, C.; Sun, X.; Burns, R. L.; Farrell, R. A.; Hetzer, D. R.; Metz, A. W.; Ko, A.; Scheer, S. A.; Biolsi, P.; DeVillers, A. EPE Improvement Thru Self-Alignment *via* Multi-Color Material Integration. In *Optical Microlithography XXX*; Erdmann, A., Kye, J., Eds.; The International Society for Optics and Photonics (SPIE), 2017; Vol. *10147*, p 1014704.
(5) Levinson, H. J. *The Potential of EUV Lithography*. In *35th European Mask and Lithography Conference (EMLC 2019)*; Behringer, U. F., Finders, J., Eds.; The International Society for Optics and Photonics (SPIE), 2019; Vol. *1117702*, p 2.
(6) Bally-Le Gall, F.; Friedmann, C.; Heinke, L.; Arslan, H.; Azucena, C.; Welle, A.; Ross, A. M.; Wöll, C.; Lahann, J. Free-Standing Nanomembranes Based on Selective CVD Deposition of Functional Poly-p-Xylylenes. *ACS Nano* **2015**, *9*, 1400−1407.
(7) Gladfelter, W. L. Selective Metallization by Chemical Vapor Deposition. *Chem. Mater.* **1993**, *5*, 1372−1388.
(8) Claassen, W. A. P.; Bloem, J. The Nucleation of CVD Silicon on SiO2 and Si3N4 Substrates: I. The System at High Temperatures. *J. Electrochem. Soc.* **1980**, *127*, 194−202.
(9) Fitch, J. T.; Denning, D. J.; Beard, D. The Pattern Dependence of Selectivity in Low Pressure Selective Epitaxial Silicon Growth. *J. Electron. Mater.* **1992**, *21*, 455−462.
(10) Hartmann, J. M.; Bertin, F.; Rolland, G.; Laugier, F.; Semeria, M. N. Selective Epitaxial Growth of Si and SiGe for Metal Oxide Semiconductor Transistors. *J. Cryst. Growth* **2003**, *259*, 419−427.
(11) Gates, S. M. Surface Chemistry in the Chemical Vapor Deposition of Electronic Materials. *Chem. Rev.* **1996**, *96*, 1519−1532.
(12) Minaye Hashemi, F. S.; Prasittichai, C.; Bent, S. F. Self-Correcting Process for High Quality Patterning by Atomic Layer Deposition. *ACS Nano* **2015**, *9*, 8710−8717.
(13) Mameli, A.; Merkx, M. J. M.; Karasulu, B.; Roozeboom, F.; Kessels, W. E. M. M.; MacKus, A. J. M. Area-Selective Atomic Layer Deposition of SiO2 Using Acetylacetone as a Chemoselective Inhibitor in an ABC-Type Cycle. *ACS Nano* **2017**, *11*, 9303−9311.
(14) Pattison, T. G.; Hess, A. E.; Arellano, N.; Lanzillo, N.; Nguyen, S.; Bui, H.; Rettner, C.; Truong, H.; Friz, A.; Topuria, T.; Fong, A.; Hughes, B.; Tek, A. T.; DeSilva, A.; Miller, R. D.; Qiao, G. G.; Wojtecki, R. J. Surface Initiated Polymer Thin Films for the Area Selective Deposition and Etching of Metal Oxides. *ACS Nano* **2020**, *14*, 4276−4288.
(15) Cho, T. H.; Farjam, N.; Allemang, C. R.; Pannier, C. P.; Kazyak, E.; Huber, C.; Rose, M.; Trejo, O.; Peterson, R. L.; Barton, K.; Dasgupta, N. P. Area-Selective Atomic Layer Deposition Patterned by Electrohydrodynamic Jet Printing for Additive Manufacturing of Functional Materials and Devices. *ACS Nano* **2020**, *14*, 17262−17272.
(16) Song, S. K.; Saare, H.; Parsons, G. N. Integrated Isothermal Atomic Layer Deposition/Atomic Layer Etching Super-Cycles for Area-Selective Deposition of TiO2. *Chem. Mater.* **2019**, *31*, 4793−4804.
(17) Leskelä, M.; Ritala, M. Atomic Layer Deposition (ALD): From Precursors to Thin Film Structures. *Thin Solid Films* **2002**, *409*, 138−146.
(18) Parsons, G. N.; George, S. M.; Knez, M. Progress and Future Directions for Atomic Layer Deposition and ALD-Based Chemistry. *MRS Bull.* **2011**, *36*, 865−871.
(19) Holleman, J. Selective Chemical Vapor Deposition. In *Chemical Physics of Thin Film Deposition Processes for Micro- and Nano-Technologies*; Pauleau, Y., Ed.; Springer: New York, 2002; pp 171−198. DOI: 10.1007/978-94-010-0353-7_8
(20) Madar, R.; Bernard, C. Thermodynamic Modeling of Selective Chemical Vapor Deposition Processes in Microelectronic Silicon. *J. Vac. Sci. Technol., A* **1990**, *8*, 1413−1421.
(21) Carlsson, J. O. Selective Vapor-Phase Deposition on Patterned Substrates. *Crit. Rev. Solid State Mater. Sci.* **1990**, *16*, 161−212.
(22) Juppo, M.; Vehkamäki, M.; Ritala, M.; Leskelä, M. Deposition of Molybdenum Thin Films by an Alternate Supply of MoCl5 and Zn. *J. Vac. Sci. Technol., A* **1998**, *16*, 2845−2850.
(23) Myers, T. J.; Cano, A. M.; Lancaster, D. K.; Clancey, J. W.; George, S. M. Conversion Reactions in Atomic Layer Processing with Emphasis on ZnO Conversion to Al 2 O 3 by Trimethylaluminum. *J. Vac. Sci. Technol., A* **2021**, *39*, 021001.
(24) Agbenyeke, R. E.; Han, S. H.; Park, B. K.; Chung, T.-M.; Lee, Y. K.; Kim, C. G.; Han, J. H. Simultaneous Etching of Underlying Metal Oxide and Sulfide Thin Films during Cu2S Atomic Layer Deposition. *Appl. Surf. Sci.* **2020**, *524*, 146452.
(25) Haukka, S. P.; Matero, R. H.; Tois, E.; Niskanen, A.; Tuominen, M.; Huotari, H.; Pore, V. J. Dual Selective Deposition. U.S. Patent Application US 2015/0299848 Al, 2015.
(26) Lemaire, P. C.; King, M.; Parsons, G. N. Understanding Inherent Substrate Selectivity during Atomic Layer Deposition: Effect of Surface Preparation, Hydroxyl Density, and Metal Oxide Composition on Nucleation Mechanisms during Tungsten ALD. *J. Chem. Phys.* **2017**, *146*, 052811.
(27) Kalanyan, B.; Losego, M. D.; Oldham, C. J.; Parsons, G. N. Low-Temperature Atomic Layer Deposition of Tungsten Using Tungsten Hexafluoride and Highly-Diluted Silane in Argon. *Chem. Vap. Deposition* **2013**, *19*, 161−166.
(28) Lemaire, P. C.; King, M.; Parsons, G. N. Understanding Inherent Substrate Selectivity during Atomic Layer Deposition: Effect of Surface Preparation, Hydroxyl Density, and Metal Oxide Composition on Nucleation Mechanisms during Tungsten ALD. *J. Chem. Phys.* **2017**, *146*, 052811.
(29) Lemaire, P. C.; Parsons, G. N. Thermal Selective Vapor Etching of TiO2: Chemical Vapor Etching *via* WF6 and Self-Limiting Atomic Layer Etching Using WF6 and BCl3. *Chem. Mater.* **2017**, *29*, 6653−6665.
(30) Roine, A.; Kotiranta, T.; Eerola, H.; Lamberg, P. *HSC Chemistry*, Ver. 7.1; Oktukumpu Research Oy: Pori, Finland, 2002.
(31) Kalanyan, B.; Lemaire, P. C.; Atanasov, S. E.; Ritz, M. J.; Parsons, G. N. Using Hydrogen to Expand the Inherent Substrate Selectivity Window during Tungsten Atomic Layer Deposition. *Chem. Mater.* **2016**, *28*, 117−126.
(32) Atanasov, S. E.; Kalanyan, B.; Parsons, G. N. Inherent Substrate-Dependent Growth Initiation and Selective-Area Atomic Layer Deposition of TiO2 Using "Water-Free" Metal-Halide/Metal Alkoxide Reactants. *J. Vac. Sci. Technol., A* **2016**, *34*, 01A148.
(33) Creighton, J. R. A Mechanism for Selectivity Loss during Tungsten CVD. *J. Electrochem. Soc.* **1989**, *136*, 271.
(34) Lee, Y.; DuMont, J. W.; Cavanagh, A. S.; George, S. M. Atomic Layer Deposition of AlF3 Using Trimethylaluminum and Hydrogen Fluoride. *J. Phys. Chem. C* **2015**, *119*, 14185−14194.
(35) Zywotko, D. R.; George, S. M. Thermal Atomic Layer Etching of ZnO by a "Conversion-Etch" Mechanism Using Sequential Exposures of Hydrogen Fluoride and Trimethylaluminum. *Chem. Mater.* **2017**, *29*, 1183−1191.
(36) Warren, A.; Nylund, A.; Olefjord, I. Oxidation of Tungsten and Tungsten Carbide in Dry and Humid Atmospheres. *Int. J. Refract. Hard Met.* **1996**, *14*, 345−353.
(37) Scharf, T. W.; Prasad, S. V.; Mayer, T. M.; Goeke, R. S.; Dugger, M. T. Atomic Layer Deposition of Tungsten Disulphide Solid Lubricant Thin Films. *J. Mater. Res.* **2004**, *19*, 3443−3446.
(38) Lee, Y.; Johnson, N. R.; George, S. M. Thermal Atomic Layer Etching of Gallium Oxide Using Sequential Exposures of HF and Various Metal Precursors. *Chem. Mater.* **2020**, *32*, 5937−5948.
(39) Klaus, J. W.; Ott, A. W.; Dillon, A. C.; George, S. M. Atomic Layer Controlled Growth of Si3N4 Films Using Sequential Surface Reactions. *Surf. Sci.* **1998**, *418*, L14−L19.
(40) Lee, Y.; Huffman, C.; George, S. M. Selectivity in Thermal Atomic Layer Etching Using Sequential, Self-Limiting Fluorination and Ligand-Exchange Reactions. *Chem. Mater.* **2016**, *28*, 7657−7665.

(41) Kim, J. Y.; George, S. M. Tin Monosulfide Thin Films Grown by Atomic Layer Deposition Using Tin 2,4-Pentanedionate and Hydrogen Sulfide. *J. Phys. Chem. C* **2010**, *114*, 17597−17603.

https://doi.org/10.1021/acsnano.1c04086
ACS Nano 2021, 15, 12276−12285